Supporting Information

Spectroscopic and MD Study of Dynamic and Structural Heterogeneities in Ionic Liquids

Eric C. Wu†, Hyung J. Kim*,†,§, and Linda A. Peteanu*,†

†Department of Chemistry, Carnegie Mellon University, Pittsburgh, Pennsylvania 15213, United States

§School of Computational Sciences, Korea Institute for Advanced Study, Seoul 02455, Korea

* E-mail: hjkim@cmu.edu, peteanu@cmu.edu

I. Force field parameters

Coarse-grained force field parameters for ionic liquids were built based on OPLS-AA[1] and ionic liquid force field parameters developed by Lopes and Padua.[2] In this coarse-grained model, hydrogen atoms and fluorine atoms are combined with the nearest atom, therefore, PF_6, $–CF_3$, $–CH_3$, and $–CH_2–$ are modeled as spheres. The partial charges of the spheres are the sum of the partial charges of the individual atoms. The Lennard-Jones (LJ) parameters of the central atom are used as the initial guess for the LJ parameters of the sphere. They are then adjusted until the structure of the coarse-grained model matches the structure produced by the all-atom model. For OPLS, dihedral potentials are modeled using the Ryckaert-Bellemans functions:

$$V_{RB}(\phi_{ijkl}) = \sum_{n=0}^{5} C_n[\cos(\psi)]^n$$

The dihedral parameters are adjusted such that the distribution of dihedrals angles for coarse-grained model matches that of the all-atom model.

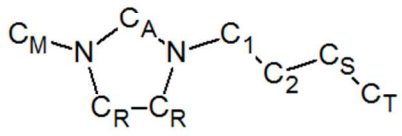

Lennard-Jones Potential and Charges

Atom	Charge	σ (nm)	ϵ (kJ mol^{-1})
C_R	0.08	0.355	0.292880
N	0.15	0.325	0.711280
C_A	0.10	0.350	0.292880
C_M	0.22	0.380	0.276114
C_1	0.09	0.365	0.276114
C_2	0.13	0.365	0.276114
C_S	0.00	0.365	0.276114
C_T	0.00	0.380	0.276114

Dihedral Potential

Dihedral	C_0	C_1	C_2	C_3	C_4	C_5
C-C-C-C	-30	0	60	-60	0	0
N-C-C-C	-80	0	15	-15	0	0

Table S1. Force field parameters for the coarse-grained imidazolium cation. C_S refers to any secondary carbon (–CH_2–) that is at least 2 bonds from the imidazolium ring. C_T refers to the terminal carbon (–CH_3).

The anion, PF_6, is modeled as a single sphere with $\sigma = 0.560$ nm and $\epsilon = 0.255200$ kJ mol^{-1}, and a charge of –1 e (e = elementary charge).[3] The dynamics for the coarse-grained model were faster than that for the all-atom model at the same temperature. To account for the differences, the temperature for the coarse-grained model was scaled by a factor of 0.71 to make the dynamics the same.

$$T_{\text{coarse-grain}} = 0.71 \times T_{\text{all-atom}}$$

Coumarin 153 (C153) is the fluorescent probe used in the simulations. C153 is described using the LJ and bonded parameters in the GROMACS OPLS-AA force field[1] and the charge distributions developed by Maroncelli[4,5]. The dipole moment of the C153 model is 6.24 D in the S_0 state and 13.59 D in the S_1 state. Simulations were performed in the presence of C153 in the S_1 state. In addition to the S_1 state charge distribution, three other different charge distributions are studied: cationic C153, neutral C153, and quadrupolar C153. For the cationic C153, $+1/36$ e charge is added to each constituent atom, so that its overall charge becomes +1 e. For the neutral coumarin 153, none of the constituent atoms have partial charges. For the quadrupolar coumarin 153, the partial charges on 4 atoms (Figure S1) are changed so that the dipole moment is 0, and the quadrupole moment tensor, Q, is

$$Q = \begin{bmatrix} 2.1583 & 7.0201 & -0.2750 \\ 7.0201 & -5.2709 & -0.3181 \\ -0.2750 & -0.3181 & 3.1126 \end{bmatrix}$$

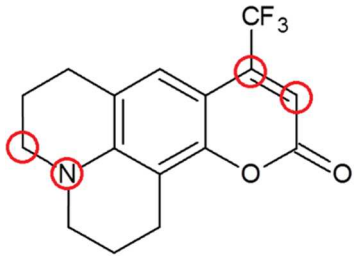

Figure S1. Structure of coumarin 153. The circled atoms are the atoms whose charges are altered in the quadrupolar coumarin 153.

II. Differences between Experiments and Simulation

The comparison between experiment and simulation necessitated several adjustments. First, simulations were performed on C153 (Figure S1) because its force field parameters are readily available.[4,5,6] However, C153 proved unsuitable for FCS measurements and yielded high background fluorescence so Nile Red (NR, Scheme 1) was used instead. As simulations correctly reproduced the width of the emission spectra of NR (Fig. S2), C153 and NR experience similar solvation environments. This validates the comparison of simulation and experiment. Second, a pyrrolidinium IL was used in experiments because, unlike imidazolium ILs, it is not fluorescent in the visible range. Finally, to ensure that the formation of non-polar regions is captured in simulation, a long-chain IL was used for modeling.[7,8] However, shorter-chain ILs were used in experiment as these have been shown experimentally to form non-polar regions.[9,10,11,12,13,14,15] Finally, to reduce the number of atoms in simulation, a smaller anion was used.

III. Nile Red Emission Spectra

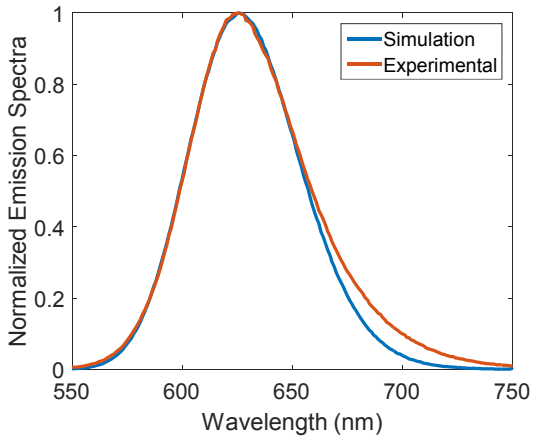

Figure S2. Simulated and experimental emission spectra of Nile Red

IV. Distribution of burst durations

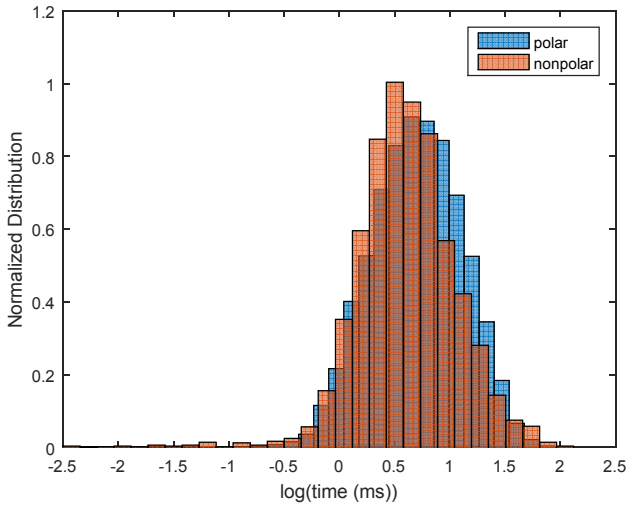

Figure S3. Distribution of nonpolar and polar burst durations

V. Residual Plots for FCS fitting

Figures S3 – S11 show the residual plots from FCS fitting. The residual plots show that the two-diffusion model and the anomalous diffusion model fit the FCS curves better than the simple diffusion (one-component) model. The oscillation observed in the residuals of the two-component fit and anomalous fit are from vibrations in the apparatus.

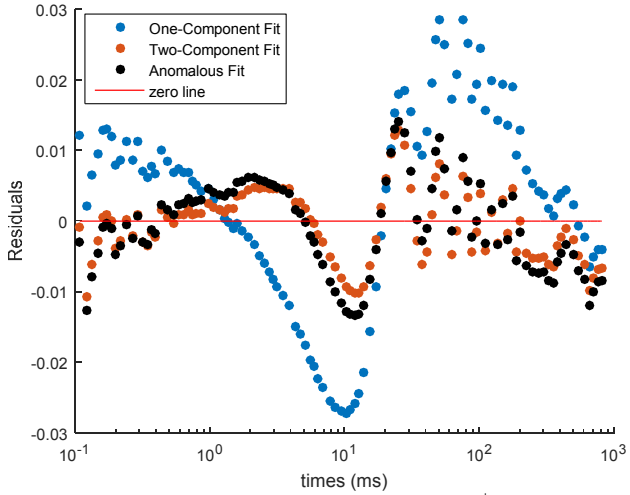

Figure S4. Residual plot for Nile Red in $Py_{14}^{+}Tf_2N^{-}$ with LP570.

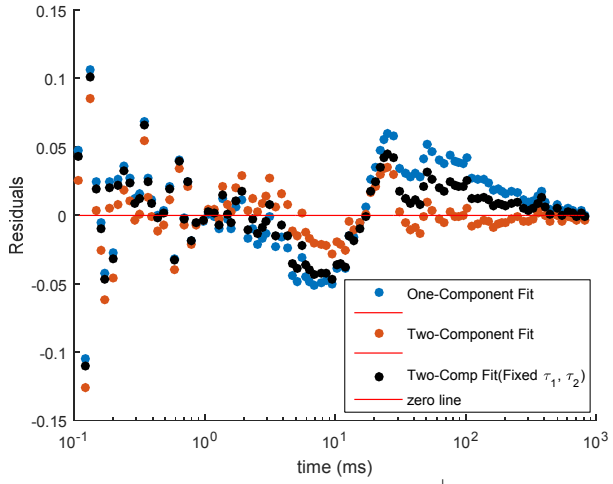

Figure S5. Residual plot for Nile Red in $Py_{14}^{+}Tf_2N^{-}$ with BP580±10.

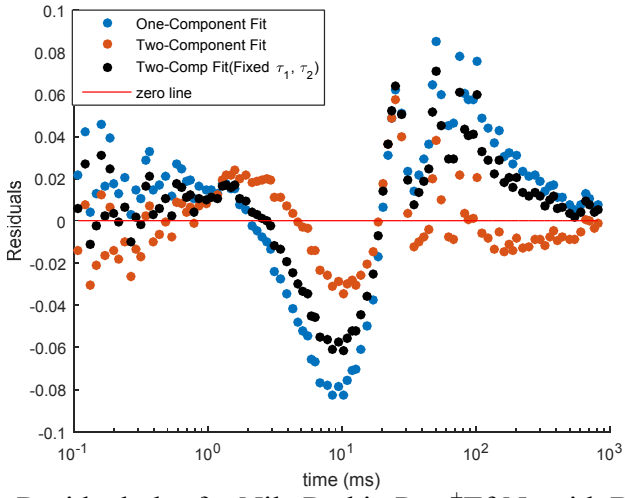

Figure S6. Residual plot for Nile Red in $Py_{14}^{+}Tf_2N^{-}$ with BP605±50.

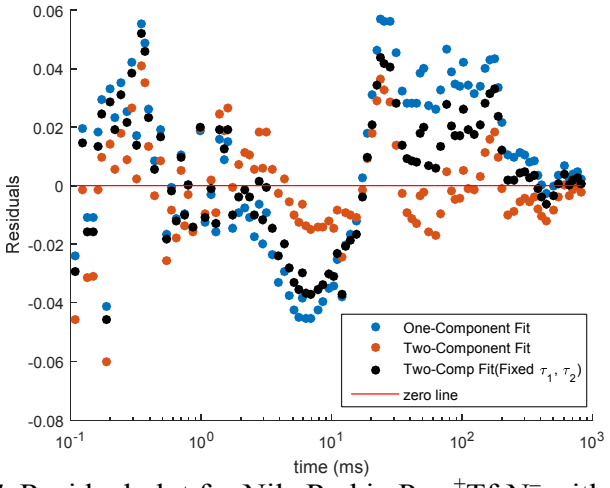

Figure S7. Residual plot for Nile Red in $Py_{14}^{+}Tf_2N^{-}$ with BP650±10.

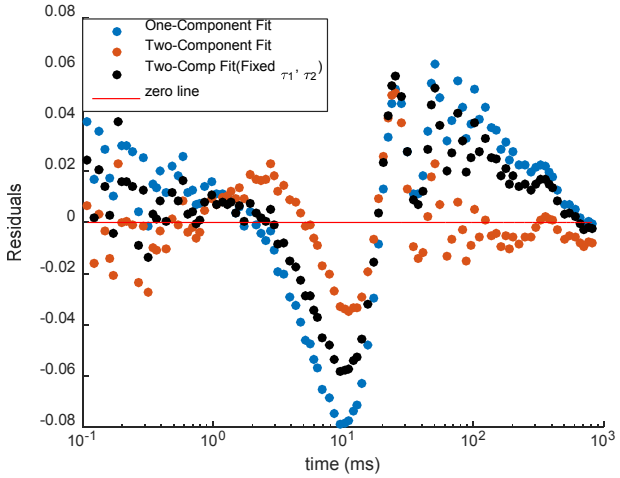

Figure S8. Residual plot for Nile Red in $Py_{14}^{+}Tf_2N^{-}$ with BP650±40.

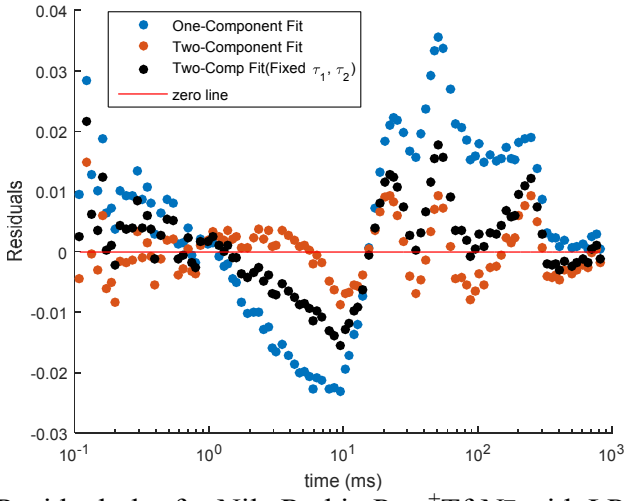

Figure S9. Residual plot for Nile Red in $Py_{14}^{+}Tf_2N^{-}$ with LP570+SP600.

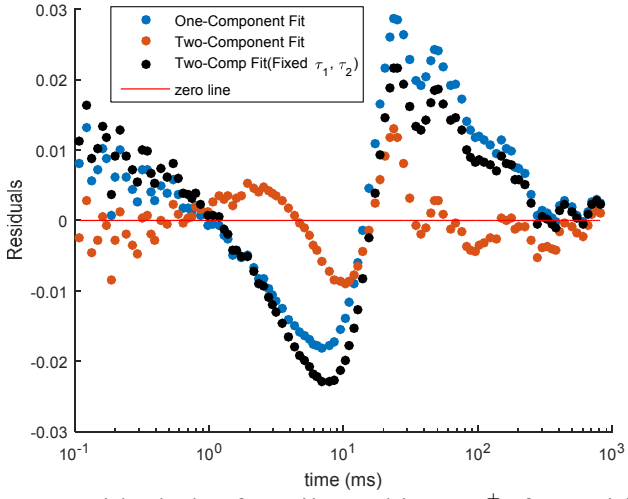

Figure S10. Residual plot for Nile Red in $Py_{14}^{+}Tf_2N^{-}$ with LP645.

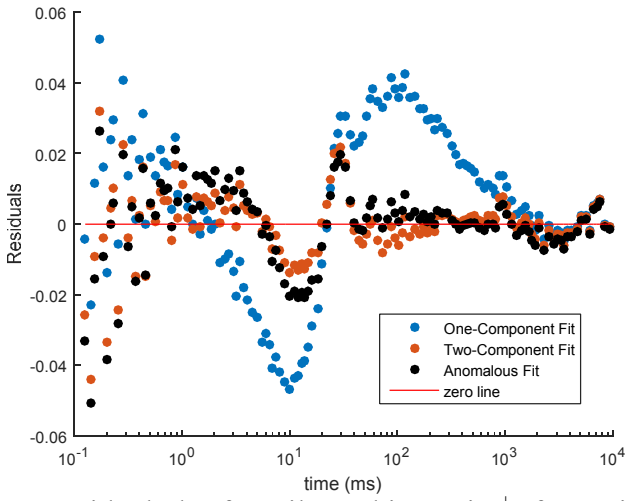

Figure S11. Residual plot for Nile Red in $Bmim^{+}Tf_2N^{-}$ with LP590.

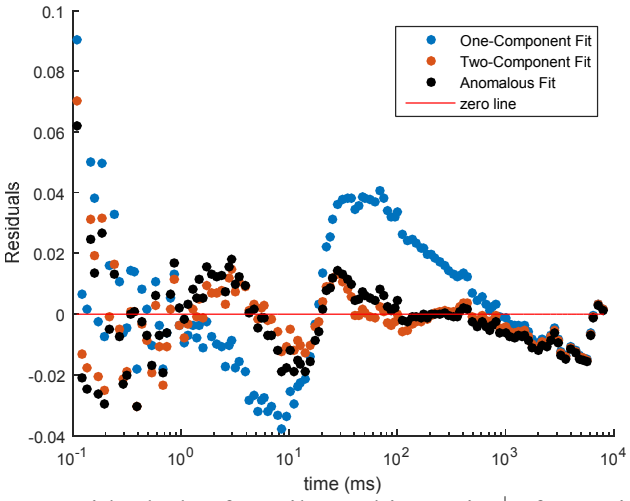

Figure S12. Residual plot for Nile Red in $Emim^{+}Tf_2N^{-}$ with LP590.

References

1 Jorgensen, W. L.; Maxwell, D. S.; Tirado-Rives, J. Development and Testing of the OPLS All-Atom Force Field on Conformational Energetics and Properties of Organic Liquids. *J. Am. Chem. Soc.* **1996**, *118*, 11225−11236.

2 Canongia Lopes, J. N.; Deschamps, J.; Pádua, A. A. H. Modeling Ionic Liquids Using a Systematic All-Atom Force Field. J. Phys. Chem. B 2004, 108, 2038−2047.

3 Jeong, D.; Choi, M. Y.; Kim, H. J.; Jung, Y. J. Fragility, Stokes-Einstein Violation, and Correlated Local Excitations in a Coarse-Grained model of an Ionic Liquid. Phys. Chem. Chem. Phys. 2010, 12, 2001–2010.

4 Roy, D.; Maroncelli, M. Simulations of Solvation and Solvation Dynamics in an Idealized Ionic Liquid Model. *J. Phys. Chem. B* **2012**, *116,* 5951 – 5970.

5 Li, H.; Arzhantsev, S.; Maroncelli, M. Solvation and Solvatochromism in CO2-Expanded Liquids. 2. Experiment-Simulation Comparisons of Preferential Solvation in Three Prototypical Mixtures. *J. Phys. Chem. B* **2007,** *111*, 3208–3221.

6. Jorgensen, W. L.; Maxwell, D. S.; Tirado-Rives, J. Development and Testing of the OPLS All-Atom Force Field on Conformational Energetics and Properties of Organic Liquids. *J. Am. Chem. Soc.* **1996**, *118*, 11225–11236.

[7] Lopes, J. N. C.; Gomes, M. F. C.; Pádua, A. A. H. Nonpolar, Polar, and Associating Solutes in Ionic Liquids. *J. Phys. Chem. B*, **2006**, *110*, 16816–16818.

[8] Wang, Y.; Voth, G. A. Tail Aggregation and Domain Diffusion in Ionic Liquids. *J. Phys. Chem. B*, **2006**, *110*, 18601–18608.

[9] Triolo, A.; Russina, O.; Blef, H.-J.; Di Cola, E. Nanoscale Segregation in Room Temperature Ionic Liquids, *J. Phys. Chem. B* **2007**, *111*, 4641–4644.

[10] Atkin, R.; Warr, G. G. The Smallest Amphiphiles: Nanostructure in Protic Room-Temperature Ionic Liquids with Short Alkyl Groups. *J Phys Chem B* **2008**, *112*, 4164–4166.

[11] Triolo. A.; Russina, O.; Fazio, B.; Triolo, R.; Di Cola, E. Morphology of 1-Alkyl-3-Methylimidazolium Hexafluorophosphate Room Temperature Ionic Liquids. *Chem. Phys. Lett.* **2008**, *457*, 362–365.

[12] Turton, D. A.; Hunger, J.; Stoppa, A.; Hefter, G.; Thoman, A.; Walther, M.; Buchner, R.; Wynne, K. Dynamics of Imidazolium Ionic Liquids from a Combined Dielectric Relaxation and Optical Kerr Effect Study: Evidence for Mesoscopic Aggregation. *J. Am. Chem. Soc.* **2009**, *131*, 11140–11146.

[13] Russina, O.; Triolo, A.; Gontrani, L.; Caminiti, R.; Xiao, D.; Hines Jr., L. G.; Bartsch, R. A.; Quitevis, E. L.; Plechkova, N.; Seddon, K. R. Morphology and Intermolecular Dynamics of 1-Alkyl-3-Methylimidazolium Bis{[trifluoromethane]sulfonyl}amide Ionic Liquids: Structural and Dynamic Evidence of Nanoscale Segregation. *J. Phys.: Condens. Matter*, **2009**, *21*, 424121.

[14] Mizoshiri, M.; Nagao, T.; Mizoguchi, Y.; Yao, M. Dielectric Permittivity of Room Temperature Ionic Liquids: A Relation to the Polar and Nonpolar Domain Structures. *J. Chem. Phys.* **2010**, *132*, 164510.

[15] Hayes, R.; Imberti, S.; Warr, G. G.; Atkin, R. Amphiphilicity Determines Nanostructure in Protic Ionic Liquids. *Phys. Chem. Chem. Phys.* **2011**, *13*, 3237–3247.